Research article

Iron-cementite nanoparticles in carbon matrix: Synthesis, structure and magnetic properties

H. Gyulasaryan [a], L. Avakyan [b], A. Emelyanov [c], N. Sisakyan [a], S. Kubrin [d], V. Srabionyan [b],
A. Ovcharov [c], C. Dannangoda [e], L. Bugaev [b], E. Sharoyan [a], M. Angelakeris [f,*], M. Farle [g],
M. Spasova [g], K. Martirosyan [e], A. Manukyan [a,*]

[a] *Institute for Physical Research, National Academy of Sciences, Ashtarak 0203, Armenia*
[b] *Physical Faculty of Southern Federal University, Zorge str., 5, Rostov-on-Don, 344090, Russia*
[c] *National Research Center "Kurchatov Institute", 1, Akademika Kurchatova sq., Moscow 123182, Russia*
[d] *Research Institute of Physics of Southern Federal University, Stachki av., 194, Rostov-on-Don, 344090, Russia*
[e] *Department of Physics and Astronomy, University of Texas at Rio Grande Valley, Brownsville, TX 78520, USA*
[f] *School of Physics Department, Aristotle University of Thessaloniki, 54124, Greece*
[g] *Faculty of Physics and Center of Nanointegration (CENIDE), University of Duisburg-Essen, Germany*

ARTICLE INFO

ABSTRACT

Carbon encapsulated iron-cementite Fe–Fe$_3$C nanoparticles with "core–shell" architecture, were synthesized by a single-step solid-state pyrolysis of iron phthalocyanine at the temperature 900 °C with pyrolysis time of 180 min. The morphology and size distribution of the fabricated nanocomposites have been investigated using high resolution transmission and scanning transmission electron microscopies which revealed Fe–Fe$_3$C nanoparticles with an average diameter of about 7.5 nm embedded in a carbon matrix. The structure, composition, and morphology of Fe–Fe$_3$C nanoparticles in the carbon matrix were analyzed by X-ray based techniques combined with Reactive Force-Field Molecular Dynamics simulations, Mössbauer spectroscopy to outline the "core–shell" architecture. Such evidence is further supported by the magnetic features of hysteresis loops at 10 and 300 K as well as the magnetization of Fe–Fe$_3$C nanoparticles is properly approximated with magnetic contributions of Fe and Fe$_3$C bulk counterparts.

1. Introduction

Nowadays magnetic nanoparticles attract much interest and are extensively studied due to their increasing applications in material science, engineering and biomedicine (magnetic resonance imaging, drug delivery and hyperthermia) [1–7]. Composite nanoparticles with "core–shell" architecture, allow the precise control of magnetic parameters by varying shape, core size and shell thickness. Particularly, bi-magnetic "core–shell" nanoparticles, where both the core and the shell exhibit magnetic properties (ferromagnetic (FM), ferrimagnetic (FiM) or antiferromagnetic (AFM)) have become of interest recently. Thus, diverse arrangements of components are possible: FM/FM, FM/AFM, FiM/AFM, FiM/FM and vice versa. They can also be classified as "hard/soft", "soft/hard" type bi-magnetic compounds, if their components have different saturation magnetizations and coercive fields. Such a combination allows to tune proximity effects and interface interactions between the core and the shell such as exchange bias (EB),

exchange coupling [8–21]. Ong et al. have analyzed Fe/Fe$_3$O$_4$ "core–shell" nanoparticle's magnetic behavior showing sharp magnetization variations on hysteresis curve at low fields [22]. They have attributed it to EB effect due to exchange interactions caused by interfacial spins between core and shell domains. Jhongi Yi. Ji. et al. investigated dynamic and static magnetizations at Ni/NiO core–shell nanoparticles measuring of exchange bias for different mean size of nanoparticles [23].

Iron carbides, especially cementite, are well known for their hardness and chemical resistance. They also attract much interest due to their tunable magnetic properties. Lipert et al. studied cementite (Fe$_3$C) nanoparticles agglomerations in carbon matrix and their magnetic properties [24]. Shajita et al. carried out synthesis of cementite nanoparticles in carbon matrix and investigated size-dependence of magnetic properties of these nanoparticles [25]. Fletcher et al. proposed a method for scalable synthesis of dispersible iron carbide nanoparticles which can be used to produce colloidal ferrofluid [26].

---

* Corresponding authors.
  E-mail addresses: agelaker@auth.gr (M. Angelakeris), manukyan.ipr@gmail.com (A. Manukyan).

Iron/iron carbide nanoparticles are also good candidates for preparing multifunctional electrocatalysts for oxygen catalysis [27].

One of most promising application of iron carbide and iron/iron carbide nanoparticles is magnetic hyperthermia, where they act as biomedical heating agents possessing high losses of magnetic energy under AC field providing high heat dissipation within tumors [28–30].

In this paper we study the structural and magnetic properties of carbon coated Fe/Fe_3C "core–shell" nanoparticles, which can be used as magnetic particle hyperthermia agents at modern cancer modalities. At first, we describe a simple one-step process for synthesis of iron-cementite "core–shell" nanoparticles surrounded by graphite-like carbon shell $Fe/Fe_3C/C$, serving as aggregation control. The synthesis was performed by solid-phase pyrolysis of iron phthalocyanine, under long pyrolysis duration (180 min) in contrast to our previous work [31] where carbon-encapsulated iron-cementite $(Fe–Fe_3C)$ nanoparticles with average weight percentage $40:60$ have been synthesized using much shorter duration solid phase pyrolysis of iron phthalocyanine. Due to the small time of pyrolysis the spread of Fe/Fe_3C concentration and the size distribution of the "core–shell" nanoparticles were larger. In the current work, the much longer (180 min) pyrolysis time together with ultrasonic treatment and size separation stages effectively lead to homogeneous narrower size distribution of nanoparticles. To obtain the structural information we performed Mössbauer, X-ray absorption near-edge structure (XANES) and extended X-ray absorption fine structure (EXAFS) spectroscopy analyses combined with Reactive Force-Field molecular dynamic (MD) simulations. The magnetic properties of the obtained nanoparticles, such as field and temperature dependencies of magnetization were studied as well by static magnetometry.

2. Synthesis of $Fe/Fe_3C/C$ and characterization methods

2.1. Samples synthesis

Carbon-encapsulated metallic nanoparticles can be conveniently synthesized using solid-phase pyrolysis of corresponding metal-phthalocyanine [32–34]. In the present study the iron-cementite Fe/Fe_3C nanoparticles in a Carbon matrix have been synthesized using solid-phase pyrolysis of iron phthalocyanine (FePc, $Pc = C_{32}N_8H_{16}$). The pyrolysis reaction can be presented in the following form [31]:

$$Fe\left(C_{32}N_8H_{16}\right) \xrightarrow[-8H_2, -4N_2]{T_{pyr}, t_{pyr}, p} Fe + 32C, \qquad (1)$$
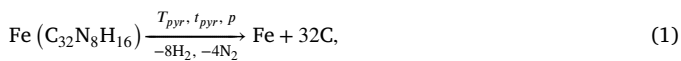
where T_{pyr} is the pyrolysis temperature (900 °C), t_{pyr} is the pyrolysis time (180 min), and p is the autogenic pressure (1.5 MPa) in the reaction ampoule. The mass percentage of the metallic component in the carbon matrix is about 12 wt%. After synthesis, ultrasonic treatment and size separation were also carried out. The first stage of pyrolysis leads to the formation of iron clusters in the carbon matrix. Then, during the growth of iron nanoparticles, surface iron atoms interact with carbon atoms and form iron carbide Fe_3C, represented by the following reaction:

$$3Fe + C \longleftrightarrow Fe_3C. \qquad (2)$$

With a long pyrolysis time (more than 9 h), a noticeable shift of reaction (2) to the left occurs [35]. Therefore, the adjustment of pyrolysis conditions should allow us to achieve both iron and cementite phases simultaneously.

2.2. Material characterization

The morphology and size distribution were investigated using a scanning transmission electron microscope (STEM) Titan 80–300 (Thermo Fisher Scientific, USA) equipped with a spherical aberration probe corrector, an energy dispersive X-ray spectrometer (EDAX, USA) and high angle annular dark field detector (Fischione, USA).

X-ray powder diffraction (XRD) experiments were performed at the mySpot beamline [36] of BESSY-II Synchrotron Radiation Facility. The powder samples were packed in a flat plate with thickness of 1 mm sealed between Kapton tape and measured in Debye–Scherrer geometry. All patterns were collected at room temperature using a monochromatic X-ray beam with the spot site of 0.5×0.5 mm^2 and wavelength $\lambda = 0.73$ Å. An image plate CCD camera (MarMosaic 225) was mounted with tilt angle ~ 0.44 degrees to the beam path with a sample to detector distance of 264 mm, as calibrated by using silver behenate and silicon standard samples. The total acquisition time for one pattern was 100 s per sample, averaged over 20 scans by 5 s each. The data averaging, and azimuthal integration to obtain $I(2\theta)$ was performed in Fit2D [37] software. The Rietveld refinement was performed using GSAS-II code [38].

X-ray absorption fine structure spectra of iron (Fe K-edge XAFS) in the powder samples $Fe–Fe_3C$ were collected in transmission mode, in the range 7.0–7.7 keV, at the BM23 beam line of the European Synchrotron Radiation Facility (ESRF). Fe K-edge XANES was measured using the photon energy scanning step $\Delta E = 0.7$ eV and Fe K-EXAFS using photoelectron wavelength step $\Delta k = 0.05$ Å^{-1}. The energy calibration was performed by Fe K-edge XAFS in the reference iron foil which was measured simultaneously with the studied samples. The initial processing of experimental Fe K-edge XAFS spectra was performed by the Demeter 0.9.26 package [39]. Fourier transformation of the extracted oscillatory parts of Fe K-EXAFS and the fitting of their Fourier transformants $F(R)$ was performed using the X-ray Larch 0.9.25 software [40] with the photoelectron scattering amplitudes and phases calculated by FEFF6 [41].

The Mössbauer spectra were recorded using the MS1104Em spectrometer with a constant acceleration mode with a helium cryostat (Janis Research CCS-850) for low-temperature measurements. The ^{57}Co(Rh) were used as a source of γ-quanta. The isomer shifts refer to α-iron.

Magnetization (M) versus temperature (T) and applied magnetic field (H) dependencies were determined using the Physical Property Measurement System (PPMS EverCool-2, Quantum Design, Inc.) with a vibrating sample magnetometer (VSM) option and the SQUID magnetometry (Quantum Design MPMS XL7). ZFC-FC sequences were recorded at the temperature range between 10 and 350 K under an applied field of 100 mT with the prior zero field cooling (ZFC) step. Typical hysteresis loops were measured at different temperatures from 10 up to 300 K for applied field ± 3 T.

3. Results and discussions

3.1. Morphology and size distribution

The STEM and high resolution TEM images (Fig. 1a, b, c) clearly outline the morphology and size distribution of iron cementite nanoparticles with a distribution of metal nanoparticles in carbon matrix. The proximity of Fe and Fe_3C densities (7.87 ± 0.01 and 7.64 ± 0.05 g cm^{-3}, respectively [42]) does not allow to distinguish these phases by TEM. Fig. 1c shows almost spherical shape of $Fe–Fe_3C$ nanoparticles, which are coated with graphite-like carbon shells (Fig. 1c). The carbon shell prevents metallic nanoparticles from further oxidation and aggregation. Fig. 1d shows the size distribution of $Fe–Fe_3C$ nanoparticles in carbon matrix and the corresponding log-normal fitting function resulting to mean diameter of particles $\langle D \rangle$ is 7.5 nm with standard deviation of $\sigma = 0.3$.

3.2. Structural features

The structural characterization of $Fe–Fe_3C$ nanoparticles in carbon matrix with average weight concentration ratio of $Fe:Fe_3C = 40:60$ obtained by the pyrolysis of short duration (3 min), was presented
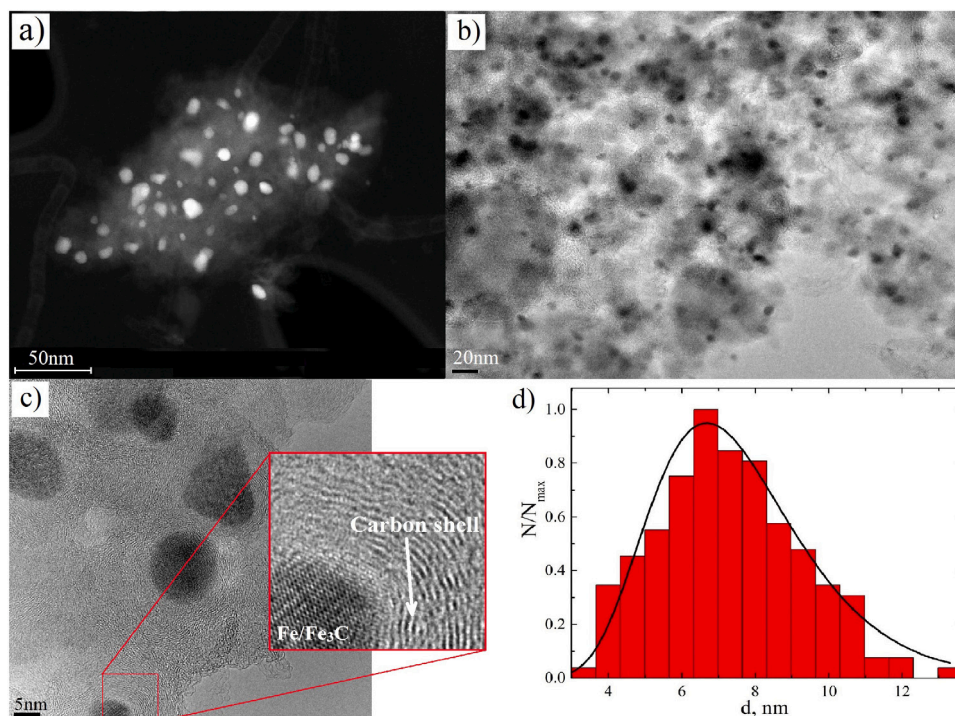
Fig. 1. STEM (a) and HRTEM (b, c) micrographs outline the spherical shape of Fe–Fe$_3$C nanoparticles capped by the carbon shell and the corresponding particle size distribution histogram (d).

Table 1
Full-profile fitting results including the weight fraction and measured lattice parameters from the XRD pattern. Reference lattice parameters from bulk materials [43] COD IDs: 2300062, 9008536 and 9008569 for Fe$_3$C, Fe and graphite, correspondingly) are shown in parentheses.

Phase	Fraction, wt%	Cell parameters, Å
Fe$_3$C, *Pnma*	8 ± 1	a = 5.053 ± 0.002 (5.085) b = 6.700 ± 0.002 (6.736) c = 4.496 ± 0.001 (4.514)
Fe, *Im3m*	5 ± 1	a = 2.847 ± 0.001 (2.867)
Graphite	87 ± 2	c = 6.833 ± 0.003 (6.696)

in details in Ref. [31] by small-angle X-ray scattering, X-ray diffraction and absorption at Fe K-edge methods combined with Reactive Force-Field molecular dynamics (MD) simulations. The details of molecular dynamics protocol for the calculation of pair radial distribution function of atoms and X-ray absorption spectrum are presented in Supplementary Material sections S1 and S2, respectively. What follows, is the overview of structural features illustrated by these methods, and confirmed by additional structural information obtained by Mössbauer spectroscopy.

3.2.1. X-ray diffraction and absorption spectroscopy

The X-ray diffraction pattern presented in Fig. 2 shows a broad peak at $2\theta \sim 12.28°$ corresponding to the graphite like carbon matrix, two peaks of α-iron ($Im3m$) at 20.88° and 29.78° and several peaks characteristic of cementite ($Pnma$).

Factually the experimental pattern (red circles) is the sum of the three components C, Fe and Fe$_3$C with a mass percentage of concentrations of 87 wt%, 5 wt% and 8 wt%, respectively. A full-profile fit, performed by theoretical patterns for 2θ within 10° to 32.5°, resulted in a good fit quality (weighted R-factor of ~3.6% and squared residual χ^2 of ~28) and gave the weight ratio of Fe and Fe$_3$C phases Fe : Fe$_3$C = 38 : 62 Fe wt.% together with corresponding cell parameters (see Table 1). The results show a 0.5–0.8% contraction of the cell parameters
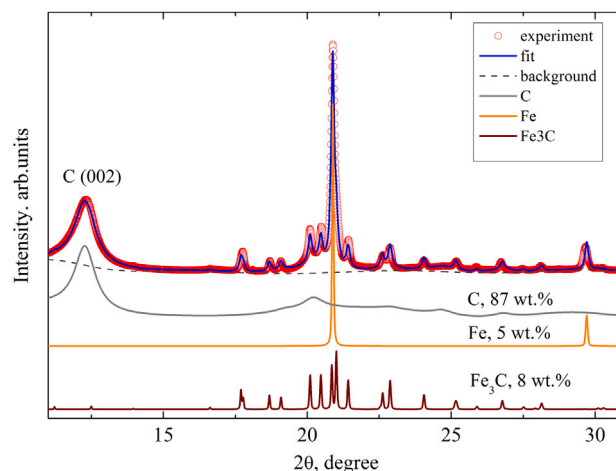

Fig. 2. Experimental (red circles) and fitted (blue line) XRD patterns. The separated spectra of graphite, iron and cementite phases with various concentrations are also shown. The dashed curve corresponds to the background contribution (polynomial fit). X-ray wavelength is 0.73 Å.

when compared with reference values at room temperature [43], as anticipated for crystalline nanoparticles due to surface tension effects.

Iron atoms may occupy sites with varying local structure environment, like in α-iron and in cementite, as suggested by XRD. Therefore, the description of Fe K-edge XANES spectrum was performed by linear combination of experimental Fe K-edge XANES spectra of bulk α-iron and cementite with weights ξ and $(1 - \xi)$ respectively, in proportion to their concentrations. The small deviations between experimental and model spectra emerged due to the difference of atomic structure in interface region of nanoparticle (shell/support and core/shell) from the structure of bulk α-iron and cementite. Fig. 3 compares the experimental and fitted Fe K-edge XANES spectra and shows their good agreement in a wide energy interval. No energy shift was introduced between iron
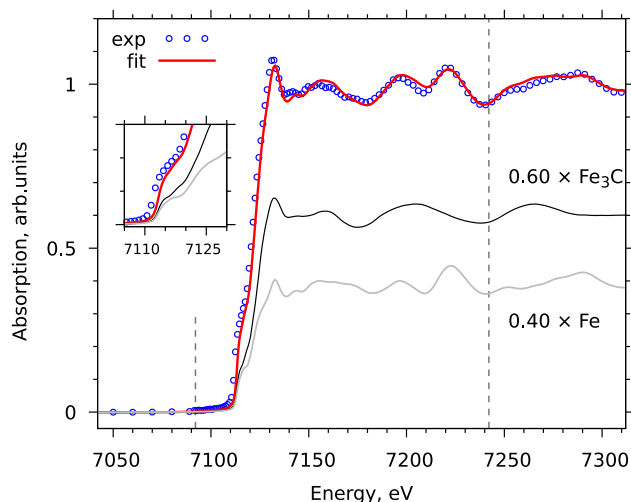
Fig. 3. Comparison of experimental Fe K-edge XANES (blue circles) and the simulated spectrum (solid red curve) obtained by linear combination of two weighted Fe K-edge XANES spectra in standards α-iron and cementite (thin gray and black curves, respectively). The fitting interval is marked by the vertical lines. Inset illustrates the zoomed region of pre-edge features.

and cementite spectra in the linear combination. The obtained ratio of iron and cementite phases $Fe : Fe_3C$ $40 : 60$ Fe at.% ($39 : 61$ wt%) with uncertainty of 2% was in qualitative agreement with that $\sim 38 : 62$ found by XRD.

In addition to the structural information derived from XRD and Fe K-edge XANES, the processing of Fe K-EXAFS spectrum gave the values of Fe–Fe and Fe–C bonds parameters: partial coordination numbers and corresponding interatomic distances, which in turn enabled to obtain pair radial distribution function (RDF) in relation to the absorbing Fe-atom, as was presented in Ref. [31]. According to the tests performed for the spectrum of α-iron foil (Figure S1 in Supplementary Material), which was used as a reference sample during measurements, the experimental Fourier-transformed EXAFS function $F(R)$ can be described up to $R = 5$ Å using the fitting model containing 4 nearest coordination shells of iron accounting for only single scattering processes. The skipping of multiple scattering processes resulted only in slightly worse description of $F(R)$ function, at $R \sim 3$ Å, though the main features of RDF remained in agreement with the experimental ones in the extended distances' range up to 5 Å. The description of experimental $F(R)$ beyond 5 Å would require accounting for more than 5 coordination shells and, probably, for higher-order photoelectron scattering processes. However, the structural information, containing in the region above 5 Å was not analyzed due to the known restrictions on the number of independently varied fit parameters [44]. We must note the recent reports of the formation of the single iron sites bounded with carbon matrix through nitrogen bridges (Fe–4N–graphite) as a result of pyrolysis of organometallic compounds [45–47]. We did not consider contribution of Fe–N bonds into the fitting model due to the high quality of the $F(R)$ fit of Fe K-EXAFS at absence of Fe–N bonds. Moreover, even if Fe–N interactions were included into the fitting model, the fraction of such Fe–N bonds, estimated from Fe K-EXAFS processing, is suited well below the conventional detection limit of $\sim 10\%$, under almost intact structural parameters of Fe–C and Fe-Fe bonds. Table S1 of supplementary material presents the obtained as a result of the fit values of structural parameters for the sample.

Fig. 4a illustrates the quality of the fit comparing magnitude of Fourier-transformed experimental Fe K-EXAFS signal ($|F(R)|$) with theoretical one. The contributions from each scattering paths (Fe–C, Fe–Fe and others) are shown with thin lines on the figure. The obtained values as a result of the fit radii of iron coordination shells 2.47, 2.84, 4.08 and 4.76 Å (uncertainties of determination are $\sim 1\%$), are

particularly close to those in the reference compound of α-iron: 2.48, 2.87, 4.05, 4.75 Å. This validates the used structural model for the fitting. The attempt of the fit without Fe–C bonds gave poor description of experimental function, especially at the left shoulder of the main peak of $|F(R)|$. The fitting of Fe K-EXAFS spectra of the sample was performed simultaneously with the fitting of the reference Fe K-EXAFS spectra of the iron foil. The last provided the reduction parameter S_0^2 (≈ 0.7) which is common for studied and for reference samples. The Kaiser–Bessel window with parameter $dk = 1$ Å^{-1} was used for the Fourier transform. The range for the fitting was set to (in R space) 1.0–5.1 Å and for the Fourier transform (in k space) to 3.5–10.5 Å^{-1}. This provided the degree of freedom $N_{idp} = 38.5$ which is well above the number of varied parameters ($N_{var} = 26$ for two spectra) used in the fit. The fitting quality is characterized by moderate R-factor of 1%.

Reactive Force Field MD simulations for Fe–Fe_3C nanoparticles revealed that the RDF is very sensitive to the most plausible combinations of the component's distribution and the particle's architecture: pure Fe and Fe_3C particles, alloyed Fe&Fe_3C structure, "core–shell" Fe@Fe_3C or inverted "core–shell" Fe_3C@Fe structures [31]. This sensitivity of RDF enabled to highlight the most suitable model of the mean particle's architecture through the comparison of simulated RDFs with the RDF derived from experimental Fe K-EXAFS spectrum. RDF derived from Fe K-EXAFS in Fe–Fe_3C sample (solid lines in Fig. 4b) is best described by RDF of "core–shell" Fe@Fe_3C nanoparticle model (boxes in Fig. 4b), similarly as it was revealed for the sample synthesized by shorter-duration pyrolysis [31].

Figure S2 in Supplementary Material presents the theoretical RDF of iron atoms in the pure iron and pure cementite nanoparticles, as well as in the "core–shell" Fe@Fe_3C and Fe_3C@Fe nanoparticles. The most noticeable in RDF differences between nanoparticle architectures are the shape of the nearest iron neighbor peak at distances of ~ 2.5 Å and the presence of peak at distance ~ 3.7 Å. The last peak is a signature of ordered cementite structures, such as pure particles or cores in layered nanoparticles. It is absent in RDF of Fe@Fe_3C nanoparticles of considered sizes and Fe : Fe_3C ratios. As a result, the RDF derived from Fe K-EXAFS in Fe-Fe3C sample (solid lines in Fig. 4b) is best described by RDF of "core–shell" Fe@Fe_3C nanoparticle model (boxes in Fig. 4b), similarly as it was revealed for the sample synthesized by shorter duration pyrolysis [31]. Fig. 4c illustrates the atomic structure of this selected model with iron core of 2.9 nm radius and cementite shell of 1.1 nm depth.

3.2.2. Mössbauer spectroscopy

Additional experimental evidence confirming the presence of the "core–shell" architecture in Fe–Fe_3C nanoparticles was obtained by means of Mössbauer spectroscopy. Fig. 5 shows the Mössbauer spectra of the Fe–Fe_3C sample measured at room temperature (RT) and 14 K. The low temperature spectrum was collected to ensure that there is no iron containing superparamagnetic impurities (such as α-FeOOH, α-Fe_2O_3 etc.) in the sample. Both room temperature and low temperature spectra exhibit similar features and consist of 3 Zeeman sextets and a singlet line.

The experimental spectra were fitted using SpectrRelax software [48] by Lorentzian peaks. The quality of the fit was verified by a χ^2 test. The hyperfine parameters of the spectra are listed in Table 2. The singlet line is caused by the impurity phase of austenite (γ-Fe) that is likely to be found in similar compounds and nanocomposites [49]. The sextet 1 isomer shift value (δ_1) corresponds to Fe ions in metallic state [50]. The quadrupole shift value (ε_1) and hyperfine magnetic field value (H_1) of sextet 1 are close to that of α-Fe Mössbauer spectrum [51]. The δ_2 and δ_3 values of the corresponding sextets are typical of Fe^{3+} ions in tetrahedral coordination [50]. The parameters of sextets 2 and 3 possess the values which are approximately equal to the parameters of the cementite Mössbauer spectrum (Fe_3C) [49,52,53]. The difference in ε values of these two sextets indicates that the Fe^{3+} ions have two types of local symmetry in cementite phases.
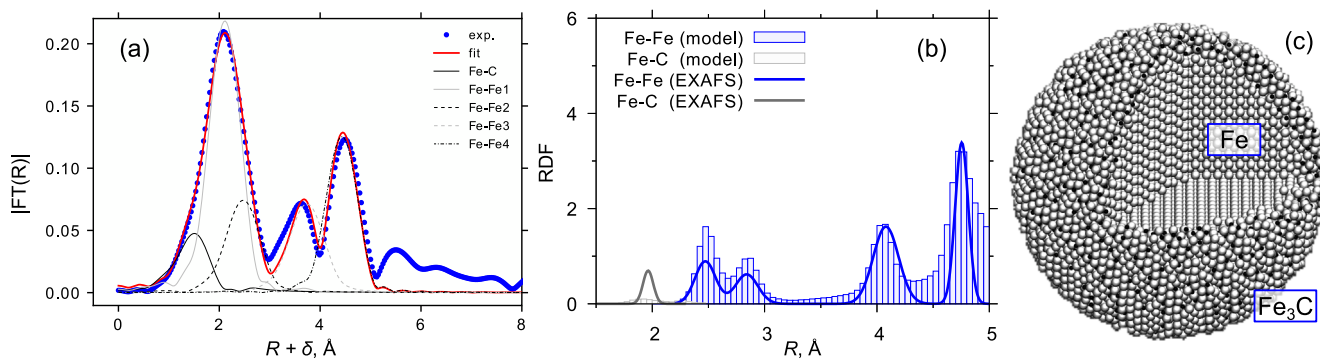
Fig. 4. Magnitude of the Fourier transform $F(R)$ of experimental Fe K-EXAFS spectrum (blue circles) is compared with the fitted one obtained by the revealed Fe–Fe and Fe–C contributions (red line) – (a); Pair radial distribution function relatively to Fe atom, calculated by the values of structural parameters of Fe–Fe and Fe–C bonds derived from experimental Fe K-EXAFS (solid curve in (b)) is compared with Reactive Force-Field MD simulated RDF (bar graphs in (b)), which corresponds to the "core–shell" Fe@Fe$_3$C architecture of mean nanoparticle schematically presented in part (c).
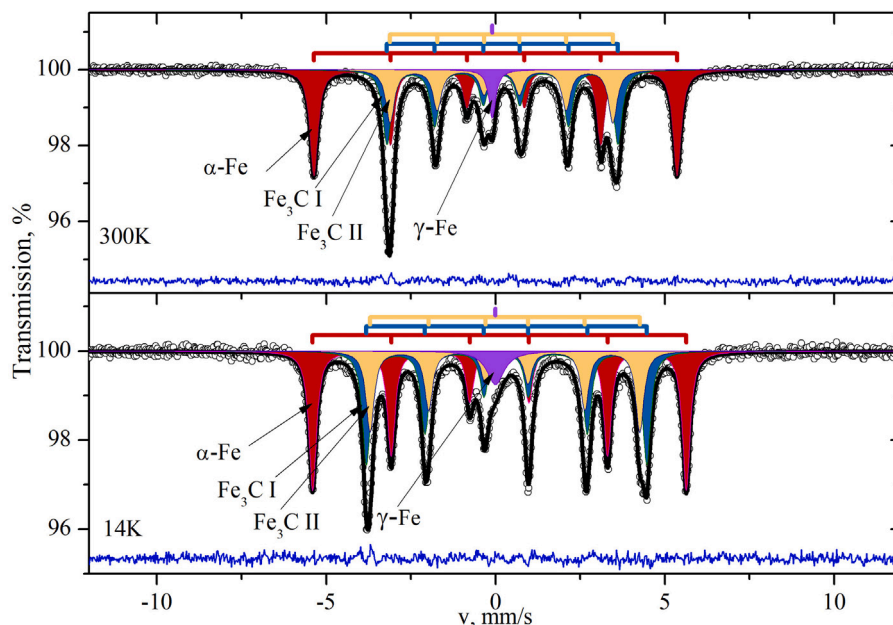

Fig. 5. Mössbauer spectra of Fe–Fe$_3$C sample measured at room temperature and 14 K.

Table 2
The parameters of Fe–Fe$_3$C Mössbauer spectra taken at room temperature and 14 K. (δ – isomer shift, ϵ – quadrupole shift, H – hyperfine magnetic field on ^{57}Fe nucleus, A – component area, G – line width, χ^2 – Pearson's criterion).

T, K	Component	$\delta \pm 0.001$, mm/s	$\epsilon \pm 0.001$, mm/s	$H \pm 0.02$, mm/s	$A \pm 0.2$, mm/s	$G \pm 0.001$, mm/s	χ^2	Fe state
300	Sextet 1	0.001	−0.001	332.61	40.1	0.287	1.446	α-Fe
	Sextet 2	0.192	0.012	211.56	32.6	0.309		Fe$_3$C I
	Sextet 3	0.178	−0.003	204.05	23.3	0.309		Fe$_3$C II
	Singlet	−0.096			4.0	0.254		γ-Fe
14	Sextet 1	0.114	0.002	342.22	38.2	0.274	1.290	α-Fe
	Sextet 2	0.320	0.007	256.77	33.1	0.291		Fe$_3$C I
	Sextet 3	0.303	−0.026	247.08	23.7	0.291		Fe$_3$C II
	Singlet	−0.002			5.0	0.618		γ-Fe

The H_3 value was found to be smaller than H_2. Since hyperfine magnetic field value depends on the number of near neighbors involved into magnetic interaction, the smaller H_3 value indicates that Fe^{3+} ions in Fe$_3$C II phase have a smaller number of Fe^{3+} as their near neighbors compared to Fe$_3$C I phase. Thus, the differences in the local symmetry of Fe^{3+} ions and hyperfine magnetic field values allow one to conclude that the sextet 2 relates to Fe$_3$C on the external layer of "core–shell"

particles, whereas the sextet 3 is associated with Fe$_3$C on the "core–shell" interface. The component area values (A) are approximately equal to the concentration of Fe ions in the corresponding phase. Therefore, about 23% of cementite are located in the "core–shell" interface. The obtained A values reveal that the iron and cementite ratio is about 40:60, which is in a good agreement with the ratio obtained from the XRD and EXAFS data.
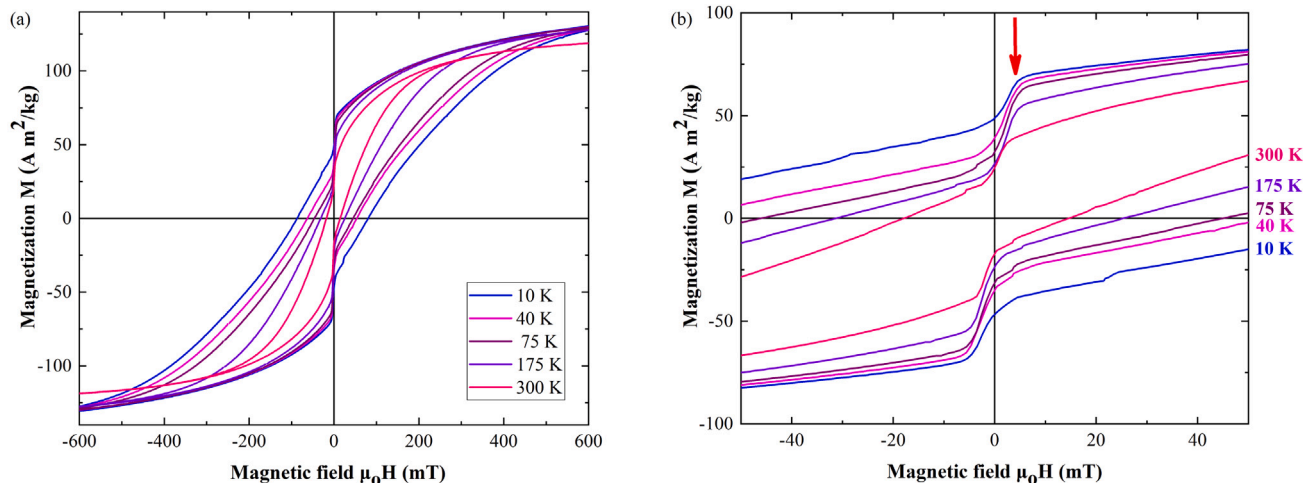
Fig. 6. (a) Magnetic hysteresis curves $M(H)$ recorded at different temperatures. (b) $M(H)$ at low field region around the origin. The arrow indicates the temperature at which the magnetization of the magnetically soft Fe core switches due to the antiferromagnetic interfacial interaction with magnetically hard Fe_3C shell.

4. Magnetic properties

Fig. 6a shows the low-field region of representative hysteresis loops of Fe–Fe_3C sample recorded at different temperatures from 10 up to 300 K for applied field ±3 T. The complete set of hysteresis loops appears at Supplementary Material as Figure S3. Magnetization values are normalized against MF which is the Magnetic Fraction consisting of two parts: Fe and Fe_3C. Sample clearly demonstrates increase of saturation magnetization with decreasing temperature from 125 A m^2 kg^{-1} at 300 K to 148 at 10 K respectively. Such behavior is determined by the transition of room temperature superparamagnetic nanoparticles to the blocking ferromagnetic state. Since the carbon magnetism is negligible, the net saturation magnetization $M_S^{(tot)}$ is the weighted average of Fe and Fe_3C saturation magnetizations:

$$M_S^{(tot)}(T) = x\% M_S^{(Fe)}(T) + (100 - x\%) M_S^{(Fe_3C)}(T) \quad (3)$$

The saturation magnetization at $T = 10K$ of Fe nanoparticles in carbon matrix can be considered approximately 210 A m^2 kg^{-1}. Since, the Fe–Fe_3C sample consists of about 40% Fe and 60% Fe_3C, the total magnetization of 148 A m^2 kg^{-1} can be approximated by (3) considering the bulk Fe_3C having a saturation magnetization of about 107 A m^2 kg^{-1} [54].

As clearly outlined in Fig. 6b, hysteresis loops recorded at different temperatures between 10 K and 300 K exhibit a narrowing at low fields and then open again. This so-called wasp-waist hysteresis loops can be attributed to variety of mechanisms [55]. In the case of nanoparticles with a broad size distribution, superposition of magnetic responses from of zero-coercivity superparamagnetic and a magnetically hard blocked single-domain nanoparticles leads a wasp-waisted shape of magnetic hysteresis loop [56]. Similar magnetic response is observed in materials composed of exchange coupled magnetically soft and magnetically hard phases such as Fe–Fe_3O_4 [22]. We may surmise that the abrupt decrease in magnetization as the field decreases (pointed by the arrow in Fig. 6b), but still with no reversal of its polarity, indicates an antiferromagnetic coupling of magnetically soft Fe (anisotropy constant $K = 5 \times 10^4$ J m^{-3}) and magnetically hard Fe_3C ($K = 2 \times 10^5$ J m^{-3}) [57] through a thin non-ordered spacer layer [58]. The coercivity of Fe–Fe_3C "core–shell" system is apparently dictated by the interactions between Fe and Fe_3C components clearly outlined by the zero-field jumps in hysteresis loops. Coercivity ($\mu_0 H_C$) ranges between 90 and 18 mT (Figs. 6a, 6b, Figure S3) within temperature range 10–300 K. The room temperature coercivity is typical for the Fe–Fe_3C nanocomposites [59].
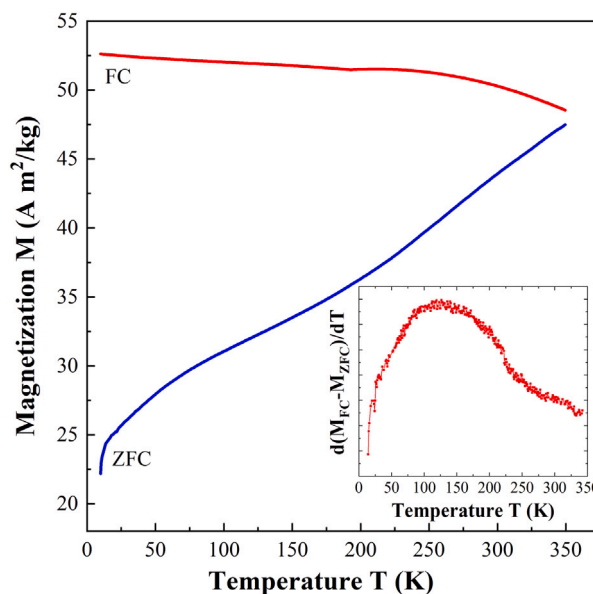

Fig. 7. Magnetization versus temperature curve of Fe–Fe_3C nanoparticles under zero-field-cooled (blue) and field-cooled (red) conditions in a field of 100 mT. Inset: $d(M_{FC} - M_{ZFC})/dT$ derivative versus temperature.

Fig. 7 shows temperature dependence of the Fe–Fe_3C sample magnetization measured under zero-field-cooled (ZFC) and field-cooled (FC) conditions in a field of 100 mT. Blocking temperature is not accurately defined due to size polydispersity and thus a mean blocking temperature value based on the temperature derivative of the FC-ZFC difference should be implemented instead [60,61]. To start with we may approximate blocking temperature T_b from the inflection point (IP) of ZFC curve resulting in a T_b value of 120 K. Although this is a rough approximation, it is in agreement with the mean $\langle T_b \rangle$ value, obtained from the universal curve of the fraction IP/$\langle T_b \rangle$ in Fig. 7 of the work by Bruvera et al. [62]. There, the value of the fraction IP/$\langle T_b \rangle$ is close to one (0.8) for magnetic nanoparticles that present the same size distribution as in our case (log-normal size distribution with a mean diameter of particles equal to 7.5 nm and a standard deviation of σ = 0.3) resulting to $\langle T_b \rangle$ = 150 K. Moreover, the derivative (inset in Fig. 7) of the difference between FC and ZFC magnetizations shows

a broad maximum around 130 K indicating the blocking temperature of the large fraction of the nanoparticles. Eventually, the blocking temperature T_b extracted from magnetometry data agrees with the TEM approximation $T_b = \frac{KV}{25k_B} = 128$ K where k_B is the Boltzmann constant, KV is the magnetic anisotropy energy, assuming magnetic anisotropy of bulk cementite, for 7.5 nm diameter nanoparticles. Nevertheless, a large fraction of the Fe–Fe$_3$C nanoparticles remain blocked with a stable magnetization direction well above room temperature. This is indicated by the hysteresis occurrence 300 K M(H) loop, as well as by the difference in ZFC and FC magnetization at 350 K (Fig. 7).

Decay of the H_c with increasing temperature for an array of non-interacting randomly oriented single-domain nanoparticles with uniaxial anisotropy is described by the Kneller's law [63]:

$$H_C(T) = H_{C_0}\left[1 - \left(\frac{T}{T_b}\right)^{1/2}\right] \tag{4}$$

where H_{C_0} is the intrinsic coercivity at $T = 0$ K and T_b is the blocking temperature of the ensemble of nanoparticles. The temperature dependence of coercivity appears at supporting material as Figure S4 together with Kneller's law fitting (according to Eq. (4) within the ferromagnetic region) yield the values for the intrinsic coercivity of H_{C_0}=120 mT and T_b=151.4 K, a value within the plateau of inset of Fig. 7. The combination of iron with cementite in nanoparticle formulation, results to tunable saturation magnetization together with coercivity when compared to typical iron-oxides rendering them as promising candidates for biomedical applications, such as magnetic particle hyperthermia [64].

5. Conclusions

In the present work iron-cementite "core–shell" nanoparticles (Fe–Fe$_3$C) in carbon matrix were synthesized using solid-phase pyrolysis of iron phthalocyanine. The STEM and HRTEM analysis showed a uniform distribution of nanoparticles in carbon matrix. The long duration pyrolysis (180 min) facilitated better size control i.e. narrower size distribution of (Fe–Fe$_3$C) nanoparticles. Iron atoms have two different types of local surrounding similar with that in α-iron and in cementite respectively. The estimated iron/cementite ratio is Fe:Fe$_3$C = 40:60.

Analysis of Fe K-EXAFS in combination with the Reactive Force Field MD simulations for nanoparticles composed of Fe and Fe$_3$C allowed to find that the most suitable structural model of mean Fe–Fe$_3$C nanoparticle is the "core–shell" architecture, consisting of Fe core and Fe$_3$C shell. Mössbauer spectra of the ICN-carbon showed that about 23% of cementite are located in the "core–shell" interface, and that the iron and cementite ratio is about 40 : 60, which is in good agreement with the ratio obtained from the analysis of XRD and K-edge XANES.

Magnetization dependence on magnetic field at 10 K and 300 K demonstrated a sudden magnetization jump at low applied fields in both positive- and negative-field sweep directions. This behavior can be associated with the "core–shell" architecture of Fe–Fe$_3$C nanoparticles with Fe and Fe$_3$C coexisting within a single particle.

CRediT authorship contribution statement

H. Gyulasaryan: Participated sufficiently in the work to take public responsibility for the content, Including participation in the concept, Design, Analysis, Writing, or Revision of the manuscript. **L. Avakyan:** Participated sufficiently in the work to take public responsibility for the content, Including participation in the concept, Design, Analysis, Writing, or Revision of the manuscript. **A. Emelyanov:** Participated sufficiently in the work to take public responsibility for the content, Including participation in the concept, Design, Analysis, Writing, or Revision of the manuscript. **N. Sisakyan:** Participated sufficiently in the work to take public responsibility for the content, Including participation in the concept, Design, Analysis, Writing, or Revision of the manuscript. **S. Kubrin:** Participated sufficiently in the work to take public responsibility for the content, Including participation in the concept, Design, Analysis, Writing, or Revision of the manuscript. **V. Srabionyan:** Participated sufficiently in the work to take public responsibility for the content, Including participation in the concept, Design, Analysis, Writing, or Revision of the manuscript. **A. Ovcharov:** Participated sufficiently in the work to take public responsibility for the content, Including participation in the concept, Design, Analysis, Writing, or Revision of the manuscript. **C. Dannangoda:** Participated sufficiently in the work to take public responsibility for the content, Including participation in the concept, Design, Analysis, Writing, or Revision of the manuscript. **L. Bugaev:** Participated sufficiently in the work to take public responsibility for the content, Including participation in the concept, Design, Analysis, Writing, or Revision of the manuscript. **E. Sharoyan:** Participated sufficiently in the work to take public responsibility for the content, Including participation in the concept, Design, Analysis, Writing, or Revision of the manuscript. **M. Angelakeris:** Participated sufficiently in the work to take public responsibility for the content, Including participation in the concept, Design, Analysis, Writing, or Revision of the manuscript. **M. Farle:** Participated sufficiently in the work to take public responsibility for the content, Including participation in the concept, Design, Analysis, Writing, or Revision of the manuscript. **M. Spasova:** Participated sufficiently in the work to take public responsibility for the content, Including participation in the concept, Design, Analysis, Writing, or Revision of the manuscript. **K. Martirosyan:** Participated sufficiently in the work to take public responsibility for the content, Including participation in the concept, Design, Analysis, Writing, or Revision of the manuscript. **A. Manukyan:** Participated sufficiently in the work to take public responsibility for the content, Including participation in the concept, Design, Analysis, Writing, or Revision of the manuscript.

Declaration of competing interest

The authors declare that they have no known competing financial interests or personal relationships that could have appeared to influence the work reported in this paper.

Data availability

The data that supports the findings of this study are available within the article and its supplementary material.

Appendix A. Supplementary data

Molecular dynamics protocol for the calculation of pair radial distribution function of atoms and X-ray absorption spectrum. Magnetic evaluation based on hysteresis loops measured from 10 to 300 K.

Supplementary material related to this article can be found online at https://doi.org/10.1016/j.jmmm.2022.169503.

References

[1] A.H. Lu, E.L. Salabas, F. Schüth, Magnetic nanoparticles: synthesis, protection, functionalization, and application, Angew. Chem. Int. Ed. 46 (2007) 1222–1244, http://dx.doi.org/10.1002/anie.200602866.

[2] Y. Bao, T. Wen, A.C. Samia, S. Sun, A. Khandhar, K.M. Krishan, Magnetic nanoparticles: Material engineering and emerging applications in Lithography and biomedicine, J. Mater. Sci. 51 (2016) 513–553, http://dx.doi.org/10.1007/s10853-015-9324-2.

[3] D.L. Leslie-Pelecky, R.D. Rieke, Magnetic properties of nanostructured materials, Chem. Mater. 8 (1996) 1770–1783, http://dx.doi.org/10.1021/cm960077f.

[4] S. Laurent, D. Forge, M. Port, A. Roch, C. Robic, L.V. Elst, R.N. Muller, Magnetic iron oxide nanoparticles: synthesis, stabilization, vectorization, physicochemical characterizations, and biological applications, Chem. Rev. 108 (2008) 110–2064, http://dx.doi.org/10.1021/cr068445e.

[5] L. Mohammed, H.G. Gomaa, D. Ragab, J. Zhu, Particuology 30 (2017) 1–14, http://dx.doi.org/10.1016/j.partic.2016.06.001.

[6] N.A. Frey, S. Peng, K. Cheng, S. Sun, Magnetic nanoparticles: synthesis, functionalization, and applications in bioimaging and magnetic energy storage, Chem. Soc. Rev. 38 (2009) 2532–2542, http://dx.doi.org/10.1039/B815548H.

[7] K. Wu, D. Su, J. Liu, R. Saha, J.-P. Wang, Magnetic nanoparticles in nanomedicine: a review of recent advances, Nanotechnology 30 (2019) 502003, http://dx.doi.org/10.1088/1361-6528/ab4241.

[8] H. Khurshid, V. Tzitzios, W. Li, C.G. Hadjipanayis, G.C. Hadjipanayis, Size and composition control of core–shell structured iron/iron-oxide nanoparticles, J. Appl. Phys. 107 (2010) 09A333, http://dx.doi.org/10.1063/1.3368720.

[9] C. Martínez-Boubeta, K. Simeonidis, M. Angelakeris, N. Pazos-Pérez, M. Giersig, A. Delimitis, L. Nalbandian, V. Alexandrakis, D. Niarchos, Critical radius for exchange bias in naturally oxidized fe nanoparticles, Phys. Rev. B 74 (2006) 054430, http://dx.doi.org/10.1103/PhysRevB.74.054430.

[10] J. Nogués, J. Sort, V. Langlais, V. Skumryev, S. Suriñach, J.S. Muñoz, M.D. Baró, Exchange bias in nanostructures, Phys. Rep. 422 (2005) 65–117, http://dx.doi.org/10.1016/j.physrep.2005.08.004.

[11] O. Iglesias, A. Labarta, X. Batlle, Exchange bias phenomenology and models of core/shell nanoparticles, J. Nanosci. Nanotechnol. 8 (2008) 2761–2780, http://dx.doi.org/10.1166/jnn.2008.18306.

[12] O. Iglesias, X. Batlle, A. Labarta, Modelling exchange bias in core/shell nanoparticles, J. Phys.: Condens. Matter 19 (2007) 406232, http://dx.doi.org/10.1088/0953-8984/19/40/406232.

[13] K. Simeonidis, C. Martinez-Boubeta, D. Serantes, S. Ruta, O. Chubykalo-Fesenko, R. Chantrell, J. Oró-Solé, L. Balcells, A.S. Kamzin, R.A. Nazipov, A. Makridis, M. Angelakeris, Controlling magnetization reversal and hyperthermia efficiency in core-shell iron-iron oxide magnetic nanoparticles by tuning the interphase coupling, ACS Appl. Nano Mater. 3 (2020) 4465–4476, http://dx.doi.org/10.1021/acsanm.0c00568.

[14] M. Estrader, A. López-Ortega, S. Estradé, I.V. Golosovsky, G. Salazar-Alvarez, M. Vasilakaki, K.N. Trohidou, M. Varela, D.C. Stanley, M. Sinko, M.J. Pechan, D.J. Keavney, F. Peiró, S. Suriñach, M.D. Baró, J. Nogués, Robust antiferromagnetic coupling in hard-soft bi-magnetic core/shell nanoparticles, Nature Commun. 4 (2013) 2960, http://dx.doi.org/10.1038/ncomms3960.

[15] E. Lottini, A. López-Ortega, G. Bertoni, S. Turner, M. Meledina, G. Van Tendeloo, C. de Julián Fernández, C. Sangregorio, Strongly exchange coupled core|shell nanoparticles with high magnetic anisotropy: A strategy toward rare-earth-free permanent magnets, Chem. Mater. 28 (2016) 4214–4222, http://dx.doi.org/10.1021/acs.chemmater.6b00623.

[16] C. Martínez-Boubeta, K. Simeonidis, D. Serantes, I. Conde-Leborán, I. Kazakis, G. Stefanou, L. Pena, R. Galceran, Ll. Balcells, C. Monty, D. Baldomir, M. Mitrakas, M. Angelakeris, Adjustable hyperthermia response of self-assembled ferromagnetic Fe-MgO core–shell nanoparticles by tuning Dipole–Dipole interactions, Adv. Funct. Mater. 22 (2012) 3737–3744, http://dx.doi.org/10.1002/adfm.201200307.

[17] F. Liu, Y. Hou, S. Gao, Exchange-coupled nanocomposites: chemical synthesis, characterization and applications, Chem. Soc. Rev. 43 (2014) 8098–8113, http://dx.doi.org/10.1039/C4CS00162A.

[18] A. López-Ortega, M. Estrader, G. Salazar-Alvarez, A.G. Roca, J. Nogués, Applications of exchange coupled bi-magnetic hard/soft and soft/hard magnetic core/shell nanoparticles, Phys. Rep. 553 (2015) 1–32, http://dx.doi.org/10.1016/j.physrep.2014.09.007.

[19] I.V. Golosovsky, G. Salazar-Alvarez, A. López-Ortega, M.A. González, J. Sort, M. Estrader, S. Suriñach, M.D. Baró, J. Nogués, Magnetic proximity effect features in antiferromagnetic/ferrimagnetic core-shell nanoparticles, Phys. Rev. Lett. 102 (2009) 247201, http://dx.doi.org/10.1103/PhysRevLett.102.247201.

[20] P.K. Manna, S.M. Yusuf, M. Basu, T. Pal, The magnetic proximity effect in a ferrimagnetic Fe₃O₄ core/ferrimagnetic γ-Mn₂O₃ shell nanoparticle system, J. Phys.: Condens. Matter 23 (2011) 506004, http://dx.doi.org/10.1088/0953-8984/23/50/506004.

[21] P.K. Manna, S.M. Yusuf, Two interface effects: Exchange bias and magnetic proximity, Phys. Rep. 535 (2014) 61–99, http://dx.doi.org/10.1016/j.physrep.2013.10.002.

[22] Q.K. Ong, A. Wei, X.-M. Lin, Exchange bias in Fe/Fe₃O₄ core–shell magnetic nanoparticles mediated by frozen interfacial spins, Phys. Rev. B. 80 (2009) 134418, http://dx.doi.org/10.1103/PhysRevB.80.134418.

[23] J.-Y. Ji, P.-H. Shih, T.-S. Chan, Y.-R. Ma, S.Y. Wu, Magnetic properties of cluster glassy Ni/NiO core–shell nanoparticles: an investigation of their static and dynamic magnetization, Nanoscale Res. Lett. 10 (2015) 243, http://dx.doi.org/10.1186/s11671-015-0925-0.

[24] K. Lipert, J. Kazmierczak, I. Pełech, U. Narkiewicz, A. Slawska-Waniewska, H. Lachowicz, Magnetic properties of cementite (Fe₃C) nanoparticle agglomerates in a carbon matrix, J. Mater. Sci.-Poland 25 (2007) 399–404.

[25] E.P. Sajitha, V. Prasad, S.V. Subramanyam, A.K. Mishra, S. Sarkar, C. Bansal, Size-dependent magnetic properties of iron carbide nanoparticles embedded in a carbon matrix, J. Phys. Condens. Matter 19 (2007) 046214, http://dx.doi.org/10.1088/0953-8984/19/4/046214.

[26] D. Fletcher, R. Hunter, W. Xia, G.J. Smales, B.R. Pauw, E. Blackburn, A. kulak, H. Xin, Z. Schnepp, Scalable synthesis of dispersible iron carbide (Fe₃C) nanoparticles by 'nanocasting', J. Mater. Chem. A 7 (2019) 19506–19512, http://dx.doi.org/10.1039/C9TA06876G.

[27] J. Jia, H. Yang, G. Wang, P. Huang, P. Cai, Z. Wen, Fe/Fe₃C nanoparticles embedded in nitrogen-doped carbon nanotubes as multifunctional electrocatalysts for oxygen catalysis and CO₂ reduction, ChemElectroChem 5 (2017) 471–477, http://dx.doi.org/10.1002/celc.201701179.

[28] A. Gangwar, S.S. Varghese, S.S. Meena, C.L. Prajapat, N. Gupta, N.K. Prasad, Fe₃C nanoparticles for magnetic hyperthermia application, J. Magn. Magn. Mater. 484 (2019) 251–256, http://dx.doi.org/10.1016/j.jmmm.2019.03.028.

[29] A. Meffre, B. Mehdaoui, V. Kelsen, P.F. Fazzini, J. Carrey, S. Lachaize, M. Respaud, B. Chaudret, A simple chemical route toward monodisperse iron carbide nanoparticles displaying tunable magnetic and unprecedented hyperthermia properties, Nano Lett. 12 (2012) 4722–4728, http://dx.doi.org/10.1021/nl302160d.

[30] A. Bordet, R.F. Landis, Y. Lee, G.Y. Tonga, J.M. Asensio, C.-H. Li, P.-F. Fazzini, K. Soulantica, V.M. Rotello, B. Chaudret, Water-dispersible and biocompatible iron carbide nanoparticles with high specific absorption rate, ACS Nano 13 (2019) 2870–2878, http://dx.doi.org/10.1021/acsnano.8b05671.

[31] L. Avakyan, A. Manukyan, A. Bogdan, H. Gyulasaryan, J. Coutinho, E. Paramonova, G. Sukharina, V. Srabionyan, E. Sharoyan, L. Bugaev, Synthesis and structural characterization of iron-cementite nanoparticles encapsulated in carbon matrix, J. Nanopart Res. 22 (2020) 30, http://dx.doi.org/10.1007/s11051-019-4698-8.

[32] A. Kocharian, H. Gyulasaryan, M. Estiphanos, M. Avramenko, K. Nelms, O. Bernal, E. Sharoyan, A. Manukyan, Ferromagnetism and giant paramagnetism of copper nanoparticles in carbon matrix, IEEE Trans. Magn. 55 (2019) 1–4.

[33] A.T. Gyulasaryan, K.A. Castillo, O.O. Bernal, A.N. Kocharian, N. Sisakyan, G.K. Chilingaryan, A.A. Veligzhanin, J.L. Gray, E.G. Sharoyan, A.S. Manukyan, Synthesis and structure of Fe-Fe₃O₄ nanoparticles with core-shell architecture capsulated in a graphite-like carbon matrix, J. Contemp. Phys. 56 (2021) 150–153, http://dx.doi.org/10.3103/S1068337221020079.

[34] A. Manukyan, A. Elsukova, A. Mirzakhanyan, H. Gyulasaryan, A. Kocharian, S. Sulyanov, M. Spasova, F. Roumer, M. Farle E. Sharoyan, Structure and size dependence of the magnetic properties of NiC nanocomposites, J. Magn. Magn. Mater. 467 (2018) 150–159, http://dx.doi.org/10.1016/j.jmmm.2018.07.056.

[35] C. Giordano, A. Kraupner, S.C. Wimbush, M. Antonietti, Iron carbide: an ancient advanced material, Small 6 (2010) 1859–1862, http://dx.doi.org/10.1002/smll.201000437.

[36] Helmholtz-Zentrum Berlin für Materialien und Energie, The myspot beamline at BESSY II, J. Large-Scale Res. Facilit. 2 (2016) A102, http://dx.doi.org/10.17815/jlsrf-2-113.

[37] A.P. Hammersley, FIT2D: A multi-purpose data reduction, analysis and visualization program, J. Appl. Crystallogr. 49 (2) (2016) 646–652, http://dx.doi.org/10.1107/S1600576716000455.

[38] B.H. Toby, R.B. Von Dreele, GSAS-II: the genesis of a modern open-source all purpose crystallography software package, J. Appl. Cryst. 46 (2013) 544–549, http://dx.doi.org/10.1107/S0021889813003531.

[39] B. Ravel, M. Newville, Athena Artemis, HEPHAESTUS: data analysis for x-ray absorption spectroscopy using IFEFFIT, J. Sync. Rad 12 (2005) 537–541, http://dx.doi.org/10.1107/S0909049505012719.

[40] M. Newville, Larch: an analysis package for XAFS and related spectroscopies, J. Phys: Conf. Ser. 430 (2013) 012007, http://dx.doi.org/10.1088/1742-6596/430/1/012007.

[41] S.I. Zabinsky, J.J. Rehr, A. Ankudinov, R.C. Albers, M.J. Eller, Multiple-scattering calculations of x-ray-absorption spectra, Phys. Rev. B 52 (1995) 2995–3009, http://dx.doi.org/10.1103/PhysRevB.52.2995.

[42] D.R. Lide, CRC Handbook of Chemistry and Physics, 88th Ed., CRC Press, ISBN: 0849304881, 2005, p. 2661.

[43] S. Gražulis, A. Daškevi, A. Merkys, D. Chateigner, L. Lutterotti, M. Quirós, N.R. Serebryanaya, P. Moeck, R.T. Downs, A. Le Bail, Crystallography open database (COD): an open-access collection of crystal structures and platform for world-wide collaboration, Nucleic. Acids. Res. 40 (2012) D420–D427, http://dx.doi.org/10.1093/nar/gkr900.

[44] L. Bugaev, L. Avakyan, V. Srabionyan, A. Bugaev, Resolution of interatomic distances in the study of local atomic structure distortions by energy-restricted x-ray absorption spectra, Phys. Rev. B 82 (2010) 064204, http://dx.doi.org/10.1103/PhysRevB.82.064204.

[45] G. Wan, X. Lin, J. Wen, W. Zhao, L. Pan, J. Tian, T. Li, H. Chen, J. Shi, Tuning the performance of single-atom electrocatalysts: Support-induced structural reconstruction, Chem. Mater. 30 (2018) 7494–7502, http://dx.doi.org/10.1021/acs.chemmater.8b02315.

[46] Y. Pan, Y. Chen, K. Wu, Z. Chen, S. Liu, X. Cao, W. Cheong, T. Meng, J. Luo, L. Zheng, C. Liu, D. Wang, Q. Peng, J. Li, C. Chen, Regulating the coordination structure of single-atom Fe-N_xC_y catalytic sites for benzene oxidation, Nature Commun. 10 (2019) 4290, http://dx.doi.org/10.1038/s41467-019-12362-8.

[47] G. Wan, G. Zhang, X. Lin, Toward efficient carbon and water cycles: Emerging opportunities with single-site catalysts made of 3d transition metals, Adv. Mater. 32 (2019) 1905548, http://dx.doi.org/10.1002/adma.201905548.

[48] M.E. Matsnev, V.S. Rusakov, SpectrRelax: An application for Mössbauer spectra modeling and fitting, AIP Conf. Proc. 1489 (2012) 178, http://dx.doi.org/10.1063/1.4759488.

[49] B. David, N. Pizúrová, O. Schneeweiss, V. Kudrle, O. Jašek, P. Synek, Iron-based nanopowders containing α-Fe, Fe_3C, and γ-Fe particles synthesised in microwave torch plasma and investigated with Mössbauer spectroscopy, Jpn. J. Appl. Phys. 50 (2011) 08JF11, http://dx.doi.org/10.1143/JJAP.50.08JF11.

[50] F. Menil, Systematic trends of the ^{57}fe mössbauer isomer shifts in (FeO_n) and (FeF_n) polyhedra. Evidence of a new correlation between the isomer shift and the inductive effect of the competing bond $\tau - \chi$ (*Fe) (where X is O or F and T any element with a formal positive charge), J. Phys. Chem. Solids 46 (1985) 763–789, http://dx.doi.org/10.1016/0022-3697(85)90001-0.

[51] R.S. Preston, S.S. Hanna, J. Heberle, Mössbauer effect in metallic iron, Phys. Rev. 128 (1962) 2207, http://dx.doi.org/10.1103/PhysRev.128.2207.

[52] G. Le Caer, J.M. Dubois, J.P. Senateur, Etude par spectrométrie Mössbauer des carbures de Fer Fe_3C et Fe_5C_2, J. Solid State Chem. 19 (1976) 19–28, http://dx.doi.org/10.1016/0022-4596(76)90145-6.

[53] J. Ma, L. Wang, Y. Deng, W. Zhang, T. Wu, Y.Song, Mass production of high-performance single atomic FeNC electrocatalysts via sequenced ultrasonic atomization and pyrolysis process, Sci. China Mater. 64 (2021) 631–641, http://dx.doi.org/10.1007/s40843-020-1464-6.

[54] D. Zhang, S. Wei, C. Kaila, X. Su, J. Wu, A. Karki, D. Young, Z. Guo, Carbon-stabilized ironnanoparticles for environmental remediation, Nanoscale 2 (2010) 917–919, http://dx.doi.org/10.1039/C0NR00065E.

[55] L.H. Bennett, E.D. Torre, Analysis of wasp-waist hysteresis loops, J. Appl. Phys. 97 (2005) 10, http://dx.doi.org/10.1063/1.1846171E502.

[56] L. Tauxe, T.A.T. Mullender, T. Pick, Potbellies, wasp-waists, and superparamagnetism in magnetic hysteresis, J. Geophys. Res.:Solid Earth 100 (1995) 17909, http://dx.doi.org/10.1029/95JB03041.

[57] S. Yamamoto, T. Terai, T. Fukuda, K.Sato, T. Kakeshita, S. Horii, M. Ito, M. Yonemura, Magnetocrystalline anisotropy of cementite pseudo single crystal fabricated under a rotating magnetic field, J. Magn. Magn. Mater. 451 (2018) 1–4, http://dx.doi.org/10.1016/j.jmmm.2017.10.114.

[58] S. Polisetty, S. Sahoo, A. Berger, Ch. Binek, Temperature dependence of the training effect in exchange coupled ferromagnetic bilayers, Phs. Rev. B 78 (2008) 184426, http://dx.doi.org/10.1103/PhysRevB.78.184426.

[59] Zh. Xu, Y. Du, D. Liu, Y. Wang, W. Ma, Y. Wang, P. Xu, X. Han, Pea-like Fe/Fe_3C nanoparticles embedded in nitrogen-doped carbon nanotubes with tunable dielectric/magnetic loss and efficient electromagnetic absorption, ACS Appl. Mater. Interfaces 11 (2019) 4268–4277, http://dx.doi.org/10.1021/acsami.8b19201.

[60] H. Mamiya, M. Ohnuma, I. Nakatani, T. Furubayashim, Extraction of blocking temperature distribution from zero-field-cooled and field-cooled magnetization curves, IEEE Trans. Magn. 41 (2005) 3394–3396, http://dx.doi.org/10.1109/TMAG.2005.855205.

[61] Y. Song, H. Modrow, L.L. Henry, C.K. Saw, E.E. Doomes, V. Palshin, J. Hormes, C.S.S.R. Kumar, Microfluidic synthesis of cobalt nanoparticles, Chem. Mater. 18 (2006) 2817–2827, http://dx.doi.org/10.1021/cm052811d.

[62] I.J. Bruvera, P. Mendoza Zélis, M. Pilar Calatayud, G.F. Goya, F.H. Sánchez, Determination of the blocking temperature of magnetic nanoparticles: The good, the bad, and the ugly, J. Appl. Phys. 118 (2015) 184304, http://dx.doi.org/10.1063/1.4935484.

[63] G.A. Candela, R.A. Haines, A method for determining the region of superparamagnetism, Appl. Phys. Lett. 34 (1979) 868, http://dx.doi.org/10.1063/1.90705.

[64] M. Angelakeris, Magnetic nanoparticles: A multifunctional vehicle for modern theranostics, Biochim. Biophys. Acta - Gen. Subj. 1861 (2017) 1642–1651, http://dx.doi.org/10.1016/j.bbagen.2017.02.022.